




# Reaction mechanism study for multinucleon transfer processes in collisions of spherical and deformed nuclei at energies near and above the Coulomb barrier: The $^{16}\text{O} + ^{154}\text{Sm}$ reaction


B. J. Roy <sup>1,2,\*</sup>, S. Santra,<sup>1,2</sup> A. Pal,<sup>1</sup> H. Kumawat,<sup>1</sup> S. K. Pandit,<sup>1</sup> V. V. Parkar <sup>1</sup>, K. Ramachandran,<sup>1</sup> K. Mahata,<sup>1</sup> and K. Sekizawa <sup>3,4,†</sup>

<sup>1</sup>*Nuclear Physics Division, Bhabha Atomic Research Centre, Mumbai 400 085, India*

<sup>2</sup>*Homi Bhabha National Institute, Anushakti Nagar, Mumbai 400 094, India*

<sup>3</sup>*Department of Physics, School of Science, Tokyo Institute of Technology, Tokyo 152-8551, Japan*

<sup>4</sup>*Nuclear Physics Division, Center for Computational Sciences, University of Tsukuba, Ibaraki 305-8577, Japan*

 (Received 2 September 2021; revised 12 November 2021; accepted 4 April 2022; published 18 April 2022)

**Background:** Multinucleon transfer reactions at energies around the Coulomb barrier offer a vital opportunity to study the rich physics of nuclear structure and dynamics, e.g., single-particle level structure and quantum shells, mass and charge equilibration processes, energy dissipation, as well as secondary decays via particle emission or fission. Despite the continuous development in the field, we still have limited knowledge about how deformation—one of the representative nuclear structures—affects multinucleon transfer reactions.

**Purpose:** To develop our understanding of the reaction mechanism and to shed light on the effect of deformation in multinucleon transfer processes, we study the  $^{16}\text{O} + ^{154}\text{Sm}$  reaction at  $E_{\text{lab}} = 85$  MeV (near the Coulomb barrier) and 134 MeV (substantially above the Coulomb barrier), where the target nucleus  $^{154}\text{Sm}$  is a well-established, deformed nucleus.

**Methods:** We have performed experiments on the  $^{16}\text{O} + ^{154}\text{Sm}$  reaction at the BARC-TIFR pelletron-Linac accelerator facility, Mumbai, India, measuring angular distributions and  $Q$ -value spectra for various transfer products. The measured cross sections have been analyzed along with theoretical calculations based on the time-dependent Hartree-Fock (TDHF) theory, together with a statistical model for secondary deexcitation processes, GEMINI++.

**Results:** Angular distributions for elastic scattering and for various transfer channels were measured over a wide angular range. The  $Q$ -value- and angle-integrated isotope production cross sections have been extracted from the measured angular distributions. We obtained production cross sections for various isotopes for  $E_{\text{lab}} = 85$  MeV, while only for four isotopes could be deduced for  $E_{\text{lab}} = 134$  MeV due to present experimental limitations. For the lower incident energy case, we find a reasonable agreement between the measurements and the TDHF calculations for a-few-nucleon transfer channels; whereas TDHF underestimates cross sections for many-nucleon transfers, consistent with earlier works. On the other side, we find that calculated cross sections for secondary reaction products for the higher incident energy case qualitatively explains the measured trends of isotopic distributions observed for the lower energy. The latter observation indicates possible underestimation of excitation energies in the present TDHF + GEMINI analysis. Although certain orientation effects were observed in TDHF results, it turns out to be difficult to disentangle them from the  $Q$ -value- and angle-integrated production cross sections.

**Conclusions:** The present analysis highlights the deep-inelastic character of multinucleon transfer processes and importance of secondary deexcitation processes. We show that the orientation effect in multinucleon transfer processes in the  $^{16}\text{O} + ^{154}\text{Sm}$  reaction is rather weak and hard to disentangle from the present measured data. Further systematic investigations, especially in the subbarrier energy regime, where the data would be more sensitive to single-particle properties, would be required to uncover effects of nuclear deformation on multinucleon transfer processes in low-energy heavy-ion reactions.

DOI: [10.1103/PhysRevC.105.044611](https://doi.org/10.1103/PhysRevC.105.044611)

## I. INTRODUCTION

The deformation of atomic nuclei plays a significant role in low-energy heavy-ion reactions. A well-established,

intuitive example is the orientation dependence of the Coulomb barrier height, which affects dramatically the fusion cross section (see, e.g., Ref. [1]). In quasifission processes, characterized by a massive nucleon transfer with zeptosecond contact time without the compound nucleus formation, the orientation of a deformed nucleus substantially alters the reaction dynamics [2–9]. When a collision occurs at equatorial side of a prolately deformed actinide nucleus, for instance, a

\*bjroy@barc.gov.in; bidyutr2003@gmail.com

†sekizawa@phys.titech.ac.jp

compact system is formed in the course of collision, leading to longer contact times with larger amount of nucleon transfer toward the mass equilibrium of the system. In tip collisions, on the other hand, an elongated dinuclear system is formed, leading to shorter contact times, while stronger shell effects are often observed. Besides, orientation-dependent inverse (or antisymmetrizing) quasifission processes have been reported for  $^{232}\text{Th} + ^{250}\text{Cf}$  [10] and  $^{238}\text{U} + ^{124}\text{Sn}$  [11]. As compared with the orientation effects in damped collisions of heavy ions, like quasifission processes, those in multinucleon transfer (MNT) processes in peripheral collisions have been less investigated so far.

There has been increasing interest in recent years in the study of MNT processes in heavy-ion reactions at energies around and above the Coulomb barrier (see, e.g., review papers [12–15] and references therein). This is partly because the MNT reaction plays a crucial role for understanding nucleon-nucleon correlations and for giving an opportunity to access a wide variety of nuclear structures in the far-off stability region. Besides, the MNT reaction between heavy ions is expected to be an efficient approach for production of neutron-rich heavy nuclei whose production is difficult by other methods [16–32], supported with promising experimental evidence [33]. The production of neutron-rich superheavy nuclei in the predicted island of stability ( $Z = 114, 120$ , or  $126$ ,  $N = 184$ ) is highly desired [34,35] because, in addition to fundamental interest in nuclear structures such as shell evolution [36] and shape transitions [37,38], it would provide a new stringent constraint for microscopic theories. The investigation of MNT processes is an important project at current and future RIB facilities such as RIBF (RIKEN, Japan) [39], HIRFL-CSR and HIAF (IMP, China) [40], RAON (RISP, Korea) [41], DRIB (FLNR, Russia), SPIRAL2 (GANIL, France) [42], FAIR (GSI, Germany) [43], SPES (INFN, Italy) [44], and FRIB (MSU, USA) [45], and so forth. It is important to provide a reliable prediction of the optimum reaction condition, such as projectile-target combinations and collision energies, to guide experiments to *terra incognita*. Since the majority of nuclei are actually deformed in their ground state, it is naturally of crucial importance to explore possible effects of mutual orientations on transfer dynamics that could also be an important factor to optimize.

In our preceding studies, we have investigated the MNT mechanism in  $^{18}\text{O} + ^{206}\text{Pb}$  [46] and  $^{16}\text{O} + ^{27}\text{Al}$  [47] reactions at energies above the Coulomb barrier. We carried out analyses of the experimental data along with theoretical calculations based on the microscopic framework of the time-dependent Hartree-Fock (TDHF) theory. As the theory based on the independent-particle picture, a detailed comparison with experimental data can offer useful information on multiparticle correlations as well as deformation and orientation dependence of MNT dynamics. In Refs. [46,47], we found reasonable agreements between measurements and TDHF calculations for  $Q$ -value- and angle-integrated transfer cross sections for both systems, where significance of secondary particle emissions were underlined. In those works,  $^{18}\text{O}$  and  $^{27}\text{Al}$  nuclei were found to be deformed in prolate and oblate shapes, respectively, in their Hartree-Fock ground state (without pairing correlations). To explore possible ori-

entation effects on MNT processes, TDHF calculations were performed for different initial orientations of those deformed nuclei, and signatures of orientation dependence were observed: (i) In the  $^{18}\text{O} + ^{206}\text{Pb}$  reaction [46], we found that neutrons could be transferred towards the opposite direction to that expected from the charge asymmetry of the system, when the deformation axis is set initially aligned to the impact-parameter vector. (ii) In the  $^{16}\text{O} + ^{27}\text{Al}$  reaction [47], we found that the colliding system shows a strong tendency towards mass equilibration, when the deformation axis is set perpendicular to the reaction plane. Although those observations are intriguing, it was not possible to see the effects in the experimental data. Also, it might be an artifact of the neglected pairing, which causes unrealistic deformation in the Hartree-Fock ground states.

A systematic investigation of MNT reactions with experimental data using different projectile-target combinations would be necessary for a better understanding of the deformation effect in the reaction mechanism. With such a motivation in mind, we report here the investigation of MNT processes in the  $^{16}\text{O} + ^{154}\text{Sm}$  reaction, where the target nucleus  $^{154}\text{Sm}$  is a well-deformed nucleus ( $\beta_2 \simeq 0.34$ ,  $E_{4+}/E_{2+} \simeq 3.25$  [48]). The experiment was carried out at the heavy-ion accelerator Pelletron-Linac facility, Mumbai, India. We set bombarding energies as  $E_{\text{lab}} = 85$  MeV (near the Coulomb barrier,  $1.1V_B$ ) and  $E_{\text{lab}} = 134$  MeV (substantially above the barrier,  $1.7V_B$ ). TDHF calculations at these two energies were performed and a detailed comparison with the measurements has been made to understand the MNT dynamics.

The article is organized as follows: In Sec. II, we describe details of the measurements and present our experimental data. In Sec. III, the results of theoretical (TDHF) calculations are presented and compared with the experimental data. A summary is given in Sec. IV.

## II. EXPERIMENTAL DETAILS

Experiments were performed at the BARC-TIFR pelletron-Linac accelerator facility, Mumbai, with an  $^{16}\text{O}$  beam. The target used was enriched  $^{154}\text{Sm}$  foil of thickness  $240 \mu\text{g}/\text{cm}^2$ . The  $^{16}\text{O} + ^{154}\text{Sm}$  reaction was studied at  $E_{\text{lab}} = 85$  and  $134$  MeV. Energy uncertainty of LINAC beam was  $\pm 0.5$  MeV. Samarium target was prepared at Radio Chemistry Division, Bhabha Atomic Research Center (BARC), Mumbai, by electro-deposition method on  $^{27}\text{Al}$  backing with backing-foil thickness of  $540 \mu\text{g}/\text{cm}^2$ . Measurements with the samarium target at all the angles were repeated by replacing samarium with pure aluminium target that was used as backing in order to subtract any contribution in the angular distribution data that may originate from aluminium backing. For detection and identification of reaction products [projectile-like fragments (PLFs)] several silicon surface barrier detector telescopes of appropriate thickness in  $\Delta E$ - $E$  configuration were used. The experimental setup and measurement details are very similar to those that we used in our earlier works [46,47], and details can be found in these references. A good charge and mass separation was achieved in  $\Delta E$ - $E$  spectrum and PLFs were identified, following standard particle identification (PI) technique as discussed in Refs. [46,47] (see Fig. 1).

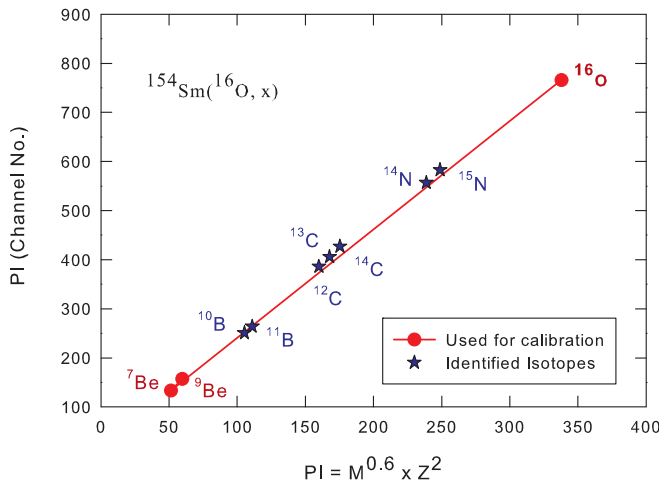


FIG. 1. Typical particle identification (PI) spectrum obtained from the  $^{16}\text{O} + ^{154}\text{Sm}$  reaction at  $E_{\text{lab}} = 85$  MeV for various projectile-like fragments.

Elastic-scattering angular distributions were measured and optical-model calculations have been carried out. Results are shown in Fig. 2 and Table I. In the figure, data are plotted along with statistical errors and in most of the cases the error bars are within the data symbols. To extract potential parameters listed in Table I, the optical-model search program SFRESKO [49] has been used and as usual a volume Woods-Saxon form is adapted for the real and imaginary parts of the potential.

At first, we carried out the optical-model analysis with the code SFRESKO for the  $E_{\text{lab}} = 85$  MeV case. The potential parameters that gave best fit (chi-squared minimization fit) to the presently measured elastic-scattering angular distribution

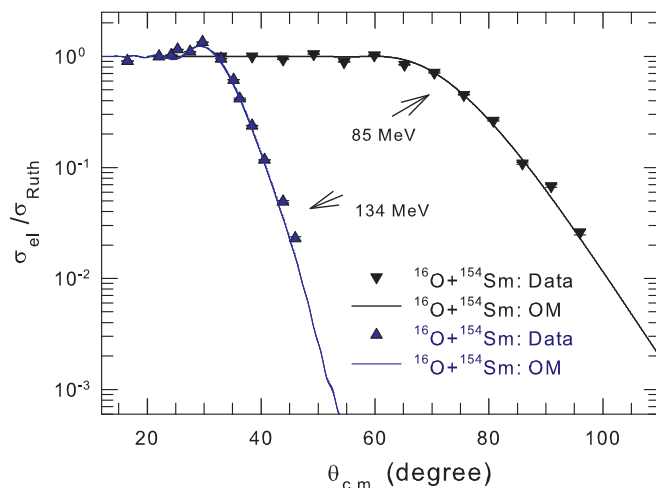


FIG. 2. The ratio of elastic scattering to the Rutherford cross sections for the  $^{16}\text{O} + ^{154}\text{Sm}$  reaction at  $E_{\text{lab}} = 85$  and 134 MeV (shown by downward and upward triangles, respectively) as a function of the scattering angle in the center-of-mass frame in degrees. Solid lines represent results of optical-model (OM) calculations with the SFRESKO code [49] for these two energies. The potential parameters obtained from the best fitting to the data are given in Table I.

TABLE I. Potential parameters for the  $^{16}\text{O} + ^{154}\text{Sm}$  reaction at  $E_{\text{lab}} = 85$  and 134 MeV, obtained from the optical-model analysis of the measured elastic-scattering angular distribution with the SFRESKO code [49].  $V$ ,  $r$ , and  $a$  ( $V_i$ ,  $r_i$ , and  $a_i$ ) represent depth, radius parameter, and diffuseness of the real (imaginary) part of the potential, respectively. The cumulative reaction cross section  $\sigma_R$  is also shown at the bottom row.

Potential parameters	$^{16}\text{O} + ^{154}\text{Sm}$ 85 MeV	$^{16}\text{O} + ^{154}\text{Sm}$ 134 MeV
$V$ (MeV)	24.0	24.1
$r$ (fm)	1.24	1.24
$a$ (fm)	0.59	0.73
$V_i$ (MeV)	17.6	16.5
$r_i$ (fm)	1.26	1.25
$a_i$ (fm)	0.68	0.72
$\sigma_R$ (mb)	1182	2357

at  $E_{\text{lab}} = 85$  MeV are shown in the second column of Table I. The cumulative reaction cross section is also listed in the bottom row of Table I. These parameters were then used as a starting potential for analyzing the  $E_{\text{lab}} = 134$  MeV data. Some variation of the potential parameters were needed to get a reasonably good agreement with the measured angular distribution at 134 MeV (Fig. 2). The best-fit potential parameters for  $E_{\text{lab}} = 134$  MeV are listed in column 3 of Table I. Significant increase in the cumulative reaction cross section, as expected, is observed upon increasing the incident energy from 85 to 134 MeV (see the bottom row of Table I).

We have derived total kinetic energy loss (TKEL) from our measured  $Q$ -value spectra, assuming a pure binary process as detailed in Ref. [46] and references therein. Obtained TKEL distributions for various transfer channels are shown in Figs. 3 and 4 for the  $E_{\text{lab}} = 85$ - and 134-MeV cases, respectively. For  $E_{\text{lab}} = 85$  MeV (Fig. 3), TKEL is low for few-nucleon transfer channels indicating dominance of quasielastic transfer. As the number of transferred nucleons increases, there is a gradual shift of the centroid of energy-loss spectra towards the larger TKEL and reaches to as large as 50 MeV for  $^6\text{Li}$ -production ( $-5p, -5n$ ) channel indicating significant contributions from deep-inelastic processes even at this lower-energy case. Note that the sharp fall- or cut-off seen at higher TKEL for some of the PLFs corresponds to the low kinetic-energy part of the PLFs that gets stopped in the  $\Delta E$  detector. There may be some contamination from aluminium backing in the TKEL spectra, however, their contribution is expected to be in the higher TKEL part because of the kinematics. In the case of  $E_{\text{lab}} = 134$  MeV (Fig. 4), we find a second bump at higher TKEL for the  $^{16}\text{O}$  channel, which is due to aluminium backing [47]. For neutron-pickup reactions ( $^{17}\text{O}$  and  $^{18}\text{O}$  PLFs), quasielastic transfer reactions predominate and the spectra are clean (any contribution from aluminium backing is hardly visible except a small bump at higher TKEL in the  $^{17}\text{O}$  spectrum, which is well separated from samarium events due to kinematics). For the channels with stripping of few nucleons (e.g.,  $^{15}\text{N}$  and  $^{14}\text{N}$  PLFs), the first peak at low TKEL corresponds to low reaction  $Q$  value, which is then followed by a strong

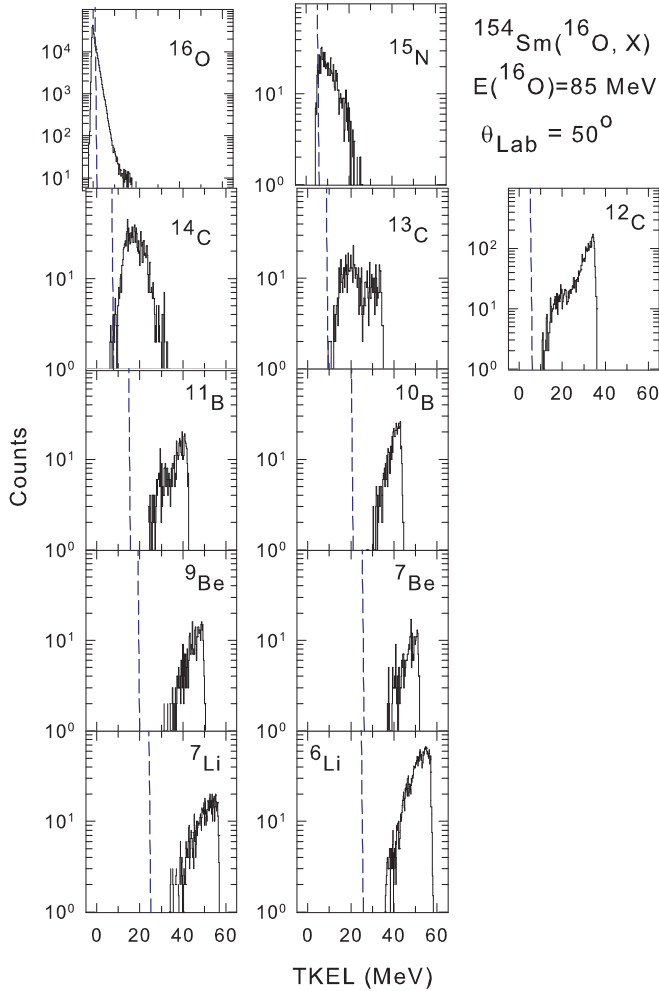


FIG. 3. Experimental total kinetic energy loss (TKEL) distributions (histogram plot) for various projectile-like fragments in the  $^{16}\text{O} + ^{154}\text{Sm}$  reaction at  $E_{\text{lab}} = 85$  MeV, at a fixed scattering angle of  $\theta_{\text{lab}} = 50^\circ$ . Vertical dashed lines indicate the ground-state  $Q$  values.

rise at larger TKEL which might be due to  $^{27}\text{Al}(^{16}\text{O}, x)$  reactions [47]. Upon further increasing the number of transferred nucleons, the energy spectra shift towards higher excitation energies and we observed a strong overlap with events from the aluminium target. It was therefore practically impossible to separate events from the pure samarium target, and hence no effort was put to extract TKEL spectra from those MNT channels.

Besides the  $Q$ -value spectra, we have also measured angular distributions for various transfer channels. By integrating over the energy,  $Q$ -value-integrated differential cross sections for various transfer channels have been obtained, and the results are shown in Fig. 5. It is to mention that the pure neutron-transfer channels in  $E_{\text{lab}} = 85$ -MeV data as well as some of other transfer channels, although visible at some of the cases at some angles, were not clearly separated (or having low counts) and hence angular distributions for those reaction channels could not be extracted. For the  $^{16}\text{O} + ^{154}\text{Sm}$  reaction at  $E_{\text{lab}} = 85$  MeV (left and middle columns in Fig. 5), the observed angular distributions are in general bell shaped,

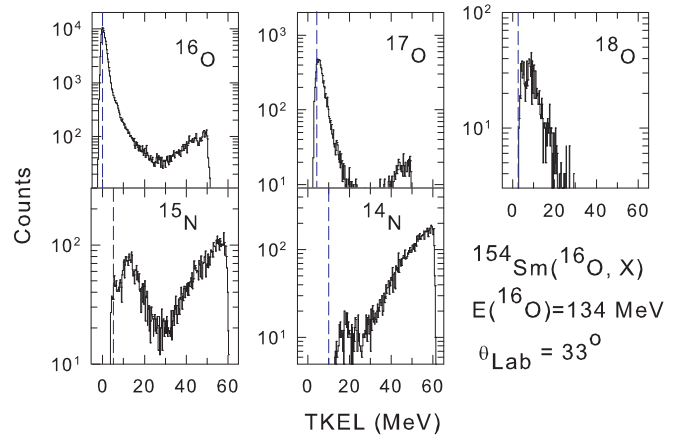


FIG. 4. Same as Fig. 3, but for  $E_{\text{lab}} = 134$  MeV at a fixed scattering angle of  $\theta_{\text{lab}} = 33^\circ$ .

peaking at an angle slightly lower than the grazing angle ( $\theta_{\text{gr}} \approx 80^\circ$  as obtained from the elastic-scattering angular distributions) with a small dependence on the reaction channel. In the case of  $E_{\text{lab}} = 134$  MeV (right column in Fig. 5), our measured data are in a limited angular range (also for a limited number of reaction channels) and the most of the data are beyond the expected peak angle (see Fig. 5). For this energy the grazing angle is  $\theta_{\text{gr}} \approx 38^\circ$ . Forward angle data were not clean and contribution from aluminium backing was relatively large, hence no effort was put to extract cross sections at those angles.

We have then obtained the  $Q$ -value- and angle-integrated total production cross sections for different transfer channels via a three-parameter Gaussian fit of the angular distributions, as detailed in Ref. [46]. Obtained isotopic production cross sections are shown in Fig. 6 for both  $E_{\text{lab}} = 85$  MeV (top and middle rows) and for 134 MeV (bottom row). Although the measured angular distributions are in a limited angular range for  $E_{\text{lab}} = 134$  MeV, as shown in Fig. 5, the three-parameter Gaussian fit was applied and total cross sections could be deduced. In the figure, cross sections for different proton-stripping channels are shown as a function of the neutron number of PLFs. In the next section, we discuss the measured cross sections in comparison with TDHF calculations.

### III. TIME-DEPENDENT HARTREE-FOCK ANALYSIS

To obtain a deeper insight into the reaction mechanism and to explore possible deformation and orientation dependence of transfer dynamics, TDHF calculations were performed for the  $^{16}\text{O} + ^{154}\text{Sm}$  reaction at  $E_{\text{lab}} = 85$  and 134 MeV. A three-dimensional parallel TDHF solver was used, which has been continuously developed since the work by Sekizawa and Yabana [50]. The code has been successfully applied to a number of systems [5, 11, 50–54], including various extensions going beyond TDHF [55–58]. In our preceding studies, we applied a TDHF analyses to our earlier experimental data for  $^{18}\text{O} + ^{206}\text{Pb}$  [46] and  $^{16}\text{O} + ^{27}\text{Al}$  [47] systems, which provide useful information for the analysis presented here. The model and calculation details have been described in the references

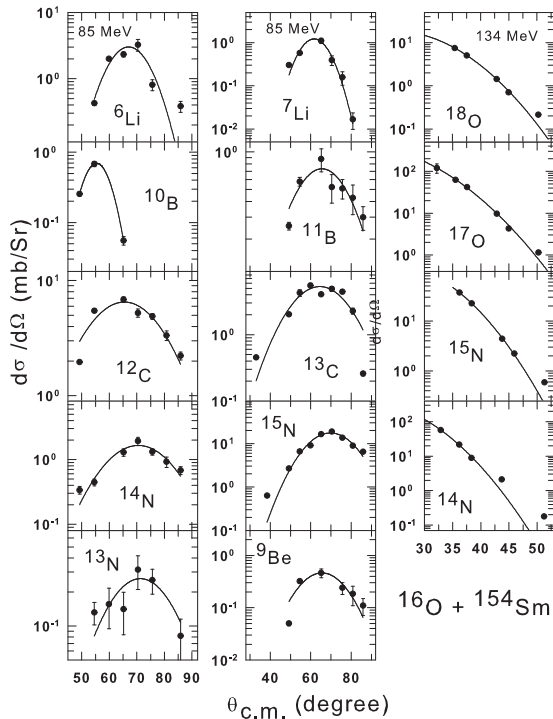


FIG. 5. Measured  $Q$ -value-integrated angular distributions for various transfer channels in the  $^{16}\text{O} + ^{154}\text{Sm}$  reaction at  $E_{\text{lab}} = 85$  MeV (the first and second columns) and 134 MeV (the third column). Solid lines represent three-parameter Gaussian fits to the data, as discussed in the text.

given above, and here we provide information relevant to the present analysis. (For details of the theoretical framework and its applications, see, e.g., review papers [14,59–64] and references therein.)

For the energy density functional, the SLy5 parameter set [65] was used, which is the same as in our preceding studies [46,47]. The Hartree-Fock ground state of  $^{16}\text{O}$  is of spherical shape, while that of  $^{154}\text{Sm}$  is largely deformed in a prolate shape ( $\beta_2 \simeq 0.32$ ), exhibiting a small octupole deformation. To explore the orientation dependence of the reaction mechanism, TDHF calculations were performed for three initial orientations of  $^{154}\text{Sm}$  as depicted in Fig. 7. The incident direction is set as the  $-x$  direction, while the impact-parameter vector is set as the  $+y$  direction, assigning the  $x$ - $y$  plane is the reaction plane. The three initial configurations considered are (i) the symmetry axis of  $^{154}\text{Sm}$  is set parallel to the collision axis ( $x$  axis), (ii) the symmetry axis is set parallel to the impact-parameter vector ( $y$  axis), and (iii) the symmetry axis is set perpendicular to the reaction plane. Henceforth, we refer to those configurations as  $x$ -,  $y$ -, and  $z$ -direction cases, respectively, throughout the paper.

Since the incident energies examined are above the Coulomb barrier, fusion reactions take place at small impact parameters. By repeating TDHF calculations the maximum impact parameters for fusion, say  $b_{\text{fus}}$ , were identified with 0.001-fm accuracy. For the  $x$ -,  $y$ -, and  $z$ -direction cases, respectively, we found:  $b_{\text{fus}} = 5.400, 6.090,$  and  $5.025$  fm for  $E_{\text{lab}} = 85$  MeV and  $b_{\text{fus}} = 7.388, 8.580,$  and  $7.208$  fm for

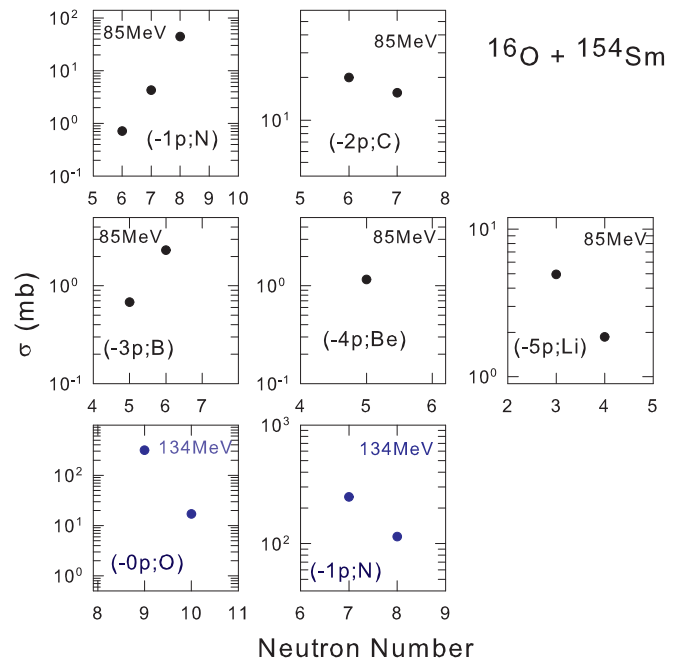


FIG. 6. The  $Q$ -value- and angle-integrated isotope production cross sections for various proton transfer channels in the  $^{16}\text{O} + ^{154}\text{Sm}$  reaction at  $E_{\text{lab}} = 85$  MeV (the first and second rows) and 134 MeV (the bottom row). The change in the number of protons compared with that of the projectile ( $Z = 8$ ) is indicated as  $(\pm xp; X)$ , where  $X$  stands for the corresponding element.

$E_{\text{lab}} = 134$  MeV. For smaller incident energies, the system requires smaller impact parameters to fuse. Also, one may notice that the fusion reaction takes place at a larger impact parameter for the  $y$ -direction case, as compared with the other two, which can be simply understood as a geometric effect (cf. Figs. 7 and 8).

In Fig. 8, we present snapshots of the density of the colliding nuclei in the reaction plane for the  $^{16}\text{O} + ^{154}\text{Sm}$  reaction at  $E_{\text{lab}} = 134$  MeV. We show two representative cases of  $x$ - and  $y$ -direction cases in Figs. 8(a) and 8(b), respectively. The elapsed time in the simulation is indicated in zeptoseconds ( $1 \text{ zs} = 10^{-21} \text{ s}$ ). In Fig. 8(a), reaction dynamics are shown for the impact parameter of  $b = 7.389$  fm, which is just outside the maximum impact parameter for fusion for the  $x$ -direction case,  $b_{\text{fus}} = 7.388$  fm. In this case,  $^{16}\text{O}$  collides with the side of  $^{154}\text{Sm}$  ( $t = 0.67$  zs), forming a neck structure. Then, the projectile-like subsystem moves along the edge of the target-like subsystem ( $t = 0.67$ – $2$  zs) and finally reseparates, forming binary fragments ( $t = 3.03$  zs). It is interesting to notice that the shape of the target-like fragment is distorted through the dynamic interaction during the collision. On the other hand, in Fig. 8(b) we show reaction dynamics for the  $y$ -direction case at the maximum impact parameter for fusion,  $b_{\text{fus}} = 8.580$  fm. In this case,  $^{16}\text{O}$  collides with the tip of  $^{154}\text{Sm}$  ( $t = 0.67$  zs). As time evolves ( $t = 1.33$ – $2.67$  zs), the system develops a neck and eventually gets fused, forming a mononuclear shape ( $t = 5.33$  zs). Figure 8 explains why in the  $y$ -direction case, the two nuclei interact at relatively large

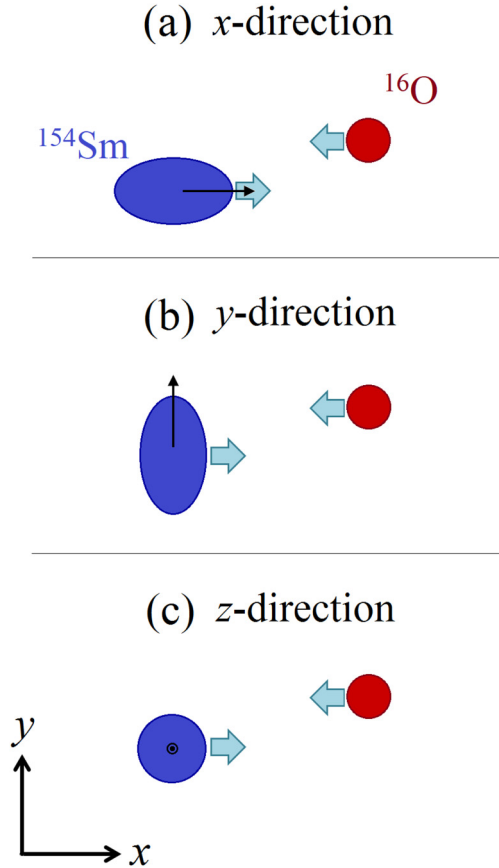


FIG. 7. A schematic illustration of three initial configurations for the  $^{16}\text{O} + ^{154}\text{Sm}$  reaction used in the TDHF calculations. Red and blue discs represent cross sections of the density of the projectile and target nuclei, respectively, in the reaction plane ( $xy$  plane). Incident direction represented by thick arrows are parallel to the  $x$  axis and the impact-parameter vector is parallel to the  $y$  axis. The three initial configurations considered are (a) symmetry axis set parallel to the collision axis ( $x$  axis), (b) symmetry axis set parallel to the impact-parameter vector ( $y$  axis), and (c) symmetry axis set perpendicular to the reaction plane.

impact parameters, while for  $x$ - and  $z$ -direction cases nucleon transfer takes place at smaller impact parameters.

Let us now look into global features of the reaction dynamics. In Figs. 9(a)–9(d) we show TKEL, the deflection function, and the average numbers of protons and neutrons, respectively, in PLFs as functions of the impact parameter. Note that we plot both results for  $E_{\text{lab}} = 85$  (134) MeV, which are represented by open (solid) symbols connected with dotted (dashed) lines. Data points with circles, triangles, and squares correspond to the  $x$ -,  $y$ -, and  $z$ -direction cases, respectively.

From Fig. 9(a), TKEL is observed to be very small when the impact parameter is large ( $b \gtrsim 7$  fm for  $E_{\text{lab}} = 85$  MeV and  $b \gtrsim 10$  fm for  $E_{\text{lab}} = 134$  MeV), corresponding to (quasi)elastic scattering. As the impact parameter decreases, TKEL increases rapidly and reaches maximum values as large as, e.g., 70 MeV for  $E_{\text{lab}} = 134$  MeV, meaning that a large amount of kinetic energy is dissipated into internal excitations after multinucleon exchanges. Around this

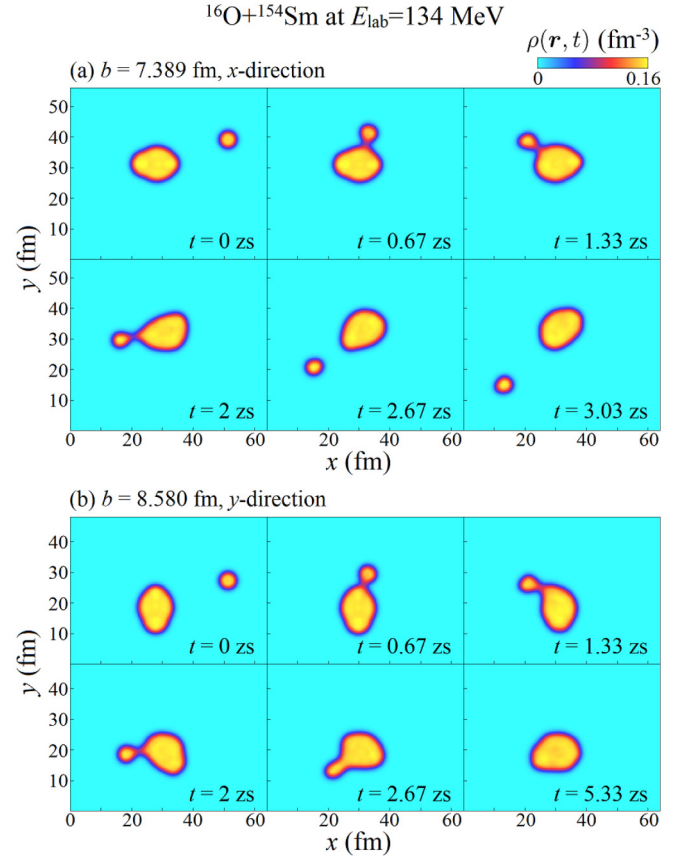


FIG. 8. Snapshots of the density of the colliding nuclei in the reaction plane obtained from the TDHF calculations for the  $^{16}\text{O} + ^{154}\text{Sm}$  reaction at  $E_{\text{lab}} = 134$  MeV. In panel (a), those for the  $x$ -direction case with  $b = 7.389$  fm (just outside the fusion threshold) are shown; while those for the  $y$ -direction case with  $b = 8.580$  fm (the maximum impact parameter for fusion) are shown in panel (b).

impact parameter, the deflection function decreases noticeably as shown in Fig. 9(b). Large negative deflection angles correspond to large scattering angles, where the trajectory of colliding nuclei is distorted by the nuclear attractive interaction. The results shown in Figs. 9(a) and 9(b) exhibit noticeable orientation dependence. Namely, TKEL (deflection function) in the  $y$ -direction case increases (decreases) at larger impact parameters as compared with the other cases. The latter is solely because of the geometry, as depicted in Fig. 8. We note that although the results look energy dependent as a function of the impact parameters, they show similar behavior when one plots as a function of the distance of the closest approach (not shown here). Thus, global feature of the reaction dynamics is almost the same for the two energies examined. Apart from the apparent geometric effect, the orientation of  $^{154}\text{Sm}$  does not alter the mean values of TKEL and  $\Theta_{\text{c.m.}}$ . It is to mention here that recent comprehensive measurements manifest good agreement between experimental data and mean TKEL and scattering angles in TDHF for deep-inelastic collisions of  $^{58}\text{Ni} + ^{58}\text{Ni}$  [55].

Next, let us look at the average numbers of protons and neutrons in PLFs shown in Figs. 9(c) and 9(d), respectively.

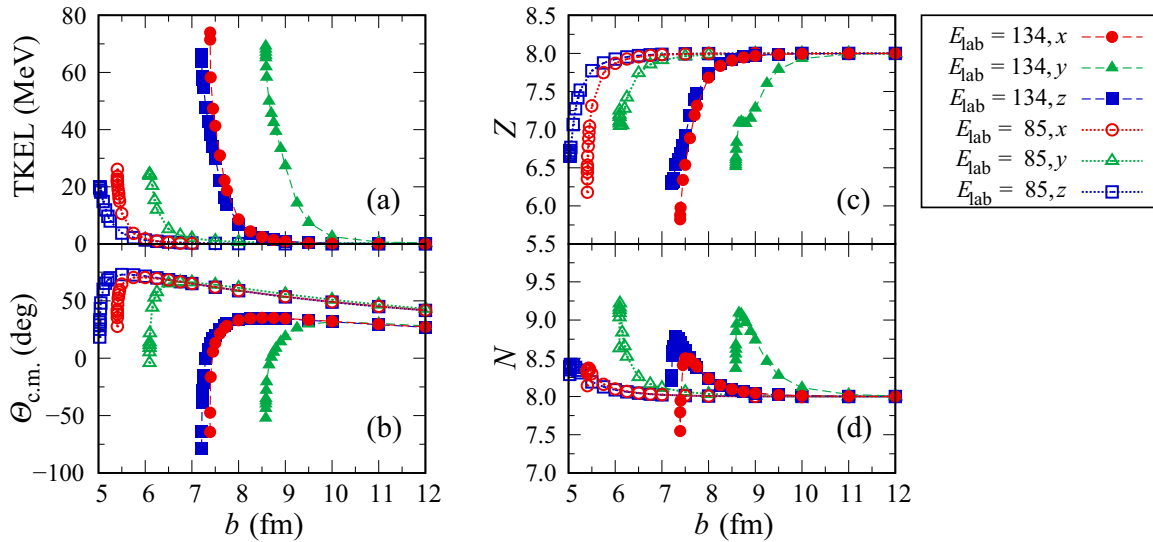


FIG. 9. Results of TDHF calculations for the  $^{16}\text{O} + ^{154}\text{Sm}$  reaction at  $E_{\text{lab}} = 85$  and  $134$  MeV. Results for  $E_{\text{lab}} = 85$  MeV are shown by open symbols connected with dotted lines, while those for  $E_{\text{lab}} = 134$  MeV are shown by solid symbols connected with dashed lines. Panels (a)–(d) show total kinetic energy loss (TKEL), deflection function, and the average numbers of protons and neutrons, respectively, in the PLF as functions of the impact parameter  $b$ .

As mentioned in the introduction, possible orientation effects on transfer dynamics were observed in our preceding studies for  $^{18}\text{O} + ^{206}\text{Pb}$  [46] and  $^{16}\text{O} + ^{27}\text{Al}$  [47]. We were thus particularly interested in understanding the effect of the large target deformation on transfer dynamics. As shown in Figs. 9(c) and 9(d), the average numbers of transferred nucleons are vanishingly small when the impact parameter is large ( $b \gtrsim 7$  fm for  $E_{\text{lab}} = 85$  MeV and  $b \gtrsim 10$  fm for  $E_{\text{lab}} = 134$  MeV), in a similar manner as was observed for TKEL and the deflection angle shown in Figs. 9(a) and 9(b). As the impact parameter decreases, nucleons are transferred towards the directions of the charge equilibrium of the system, reducing the  $N/Z$  asymmetry between projectile and target nuclei. Since the initial  $N/Z$  ratios are 1 for  $^{16}\text{O}$  and about 1.48 for  $^{154}\text{Sm}$ , neutrons tend to transfer from  $^{154}\text{Sm}$  to  $^{16}\text{O}$ , while the trend is opposite for protons. Again, we find the geometric effect also on the transfer dynamics, where nucleon transfer occurs at relatively larger impact parameters in the  $y$ -direction case as compared with the other cases.

At small impact parameters close to the fusion threshold, an abrupt change of transfer dynamics is observed, especially for  $E_{\text{lab}} = 134$  MeV. Namely, the average number of neutrons in PLFs decreases sharply [Fig. 9(d)], which also accompanies a sudden decrease of the number of protons in a correlated manner [Fig. 9(c)]. This kind of transfer dynamics has been routinely observed in TDHF for various systems [5,11,46,47,50], which can be interpreted as nucleon transfer associated with neck breaking dynamics. When two nuclei collide a neck structure is developed, during which the system evolves quickly towards the charge equilibrium through fast exchange of neutrons and protons. When the neck dissociates a correlated transfer of neutrons and protons occurs as a result of transfer of charge equilibrated matter inside the neck region. For this system, a strong tendency towards fusion gives rise to the correlated transfer of nucleons from  $^{16}\text{O}$  to

$^{154}\text{Sm}$ . In the lower incident energy case ( $E_{\text{lab}} = 85$  MeV) the abrupt change is hardly seen (symptom is visible, though), because the system could not overcome a strong tendency towards fusion after the neck formation, whereas centrifugal force enabled the system to re-separate for  $E_{\text{lab}} = 134$  MeV.

Concerning orientation dependence of transfer dynamics, other than the geometric effect, we find that neutron transfer from  $^{154}\text{Sm}$  to  $^{16}\text{O}$  is somewhat enhanced for the  $y$ -direction case [Fig. 9(d)], while proton transfer from  $^{16}\text{O}$  to  $^{154}\text{Sm}$  is enhanced for the  $x$ - and  $z$ -direction cases [Fig. 9(c)]. We will come back to this point at the end of this section, along with an additional theoretical analysis of the  $^{24}\text{O} + ^{154}\text{Sm}$  reaction.

Let us now compare measurements and theoretical calculations for total ( $Q$ -value- and angle-integrated) isotope production cross sections. In TDHF, transfer probabilities can be extracted from a TDHF wave function after collision with the use of the particle-number projection method as described in, e.g., Refs. [50,66]. Transfer cross sections are then calculated by integrating the transfer probabilities over the impact parameter. Those cross sections correspond to production of reaction products just after re-separation before secondary deexcitation processes. As the primary reaction products populated through MNT reactions could be highly excited, secondary deexcitation processes via light particle emissions may contribute significantly in the final isotope production cross sections. Such calculations are performed in a method called TDHF + GEMINI [53], which combines TDHF calculations with a statistical model, GEMINI++ [67–69]. Details of the calculations are as given in Ref. [53], while the experimental masses have been updated to AME2020 [70,71]. Because of the large mass asymmetry of the system under study, the assumption of thermal equilibrium; that is, distributing the total excitation energy proportional to the fragment masses, substantially weakens the effect of secondary evaporation from PLFs. As the experimental data indicate large

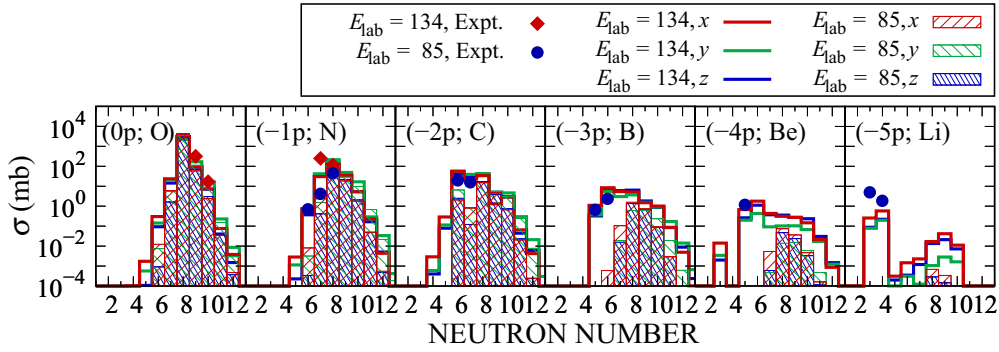


FIG. 10. The  $Q$ -value- and angle-integrated isotope production cross sections for various proton-transfer channels in the  $^{16}\text{O} + ^{154}\text{Sm}$  reaction at  $E_{\text{lab}} = 85$  and  $134$  MeV. The change in the number of protons compared with that of the projectile ( $Z = 8$ ) is indicated as  $(-xp; X)$ , where  $X$  stands for the corresponding element. Filled circles (diamonds) show the experimental data for  $E_{\text{lab}} = 85$  ( $134$ ) MeV. The results of TDHF + GEMINI calculations for  $E_{\text{lab}} = 85$  ( $134$ ) MeV are shown by shaded (open) histograms, where red, green, and blue colors are used for the  $x$ -,  $y$ -, and  $z$ -direction cases, respectively.

effects of secondary particle emissions, we distributed the excitation energy equally to the fragments, i.e.,  $E_{N,Z}^*(b) = \frac{1}{2}[E_{\text{c.m.}} - E_{\text{kin}}^\infty(b) + Q_{\text{gg}}(N, Z)]$ , which results in larger evaporation effects. Here,  $E_{\text{kin}}^\infty(b)$  denotes the asymptotic value of total kinetic energy (TKE) of outgoing fragments for average products in TDHF at an impact parameter  $b$ , and  $Q_{\text{gg}}$  is the ground-to-ground  $Q$  value for the exit channel involving a nucleus with  $N$  neutrons and  $Z$  protons.

In Fig. 10, we compare the measured integrated cross sections with the results by TDHF + GEMINI. Filled diamonds (filled circles) represent the measured cross sections for  $E_{\text{lab}} = 134$  ( $85$ ) MeV. The results of TDHF + GEMINI for  $E_{\text{lab}} = 134$  MeV are shown by open histograms, while those for  $E_{\text{lab}} = 85$  MeV are shown by shaded histograms. Red, green, and blue colors correspond to the results associated with the  $x$ -,  $y$ -, and  $z$ -direction cases, respectively. The cross sections are classified according to the number of transferred protons as indicated by  $(-xp; X)$ , where  $X$  stands for the corresponding element, and are plotted as a function of the neutron number of the reaction product.

In the case of  $E_{\text{lab}} = 134$  MeV, the experimental data are limited for  $(0p)$  and  $(-1p)$  channels with transfer of few neutrons (cf. Figs. 5 and 6). The agreement between theoretical predictions and measurements is reasonable, although the data are limited and TDHF provides somewhat smaller cross sections, especially for the  $(-1p, -1n)$  channel.

In the case of  $E_{\text{lab}} = 85$  MeV, cross sections were measured for more abundant proton-transfer channels, as compared with the  $E_{\text{lab}} = 134$  MeV case. For transfer of a few nucleons, i.e.,  $(-1p, 0n)$  and  $(-1p, -1n)$ , we again find reasonable agreement between the theoretical and experimental results. For other measured cross sections, however, TDHF substantially underestimates the experimental data, even after the inclusion of secondary deexcitation effects with GEMINI++ (compare filled circles and shaded histograms). On the other hand, we find that the cross sections for secondary products associated with  $E_{\text{lab}} = 134$  MeV (open histograms) follow nicely the trends observed in the experimental data for  $E_{\text{lab}} = 85$  MeV. Especially, production of  $^{10,11}\text{B}$ ,  $^9\text{Be}$ , and  $^{6,7}\text{Li}$  can only be explained by light-charged-particle emissions from excited

PLFs. It indicates that the effects of secondary deexcitation processes, i.e., excitation energies, may be underestimated for  $E_{\text{lab}} = 85$  MeV in the present TDHF + GEMINI analysis. Indeed, the TKEL value for mean binary products in  $E_{\text{lab}} = 85$  MeV was at most 30 MeV in TDHF [cf. Fig. 9(a)], whereas experimental TKEL distributions for  $^{10,11}\text{B}$ ,  $^9\text{Be}$ , and  $^{6,7}\text{Li}$  show substantial deep-inelastic components around  $\text{TKEL} \approx 40$ – $60$  MeV, which indicates the importance of secondary light-particle emissions.

The underestimation of excitation energy may originate from the mean-field nature of the TDHF approach. To evaluate excitation energy of reaction products, mean total excitation energy was distributed equally to the binary products. On the one hand, it has been well established that TDHF can provide quantitative description of the most probable reaction outcomes, such as average total excitation energy. On the other hand, in reality, the excitation energy has a certain distribution, meaning that part of fragments can have higher excitation energies than the mean value, for which larger evaporation effects are expected. To improve the description, one may employ a theoretical framework that incorporates beyond-TDHF fluctuations and correlations, e.g., time-dependent random-phase approximation (TDRPA) [60] which is based on an extended variational principle of Balian and Vénéroni [72] or a stochastic mean-field (SMF) approach [57,73,74]. A work on kinetic-energy distributions within the SMF approach is in progress [58].

Overall, it turns out that the orientation effects in MNT processes in the  $^{16}\text{O} + ^{154}\text{Sm}$  system is rather small, which is hard to disentangle from the integrated production cross sections, as shown in Fig. 10. We point out that the incident energies examined here are both above the Coulomb barrier for all orientations. By decreasing the incident energy, for instance, below the Coulomb barrier for collisions from the equatorial side of  $^{154}\text{Sm}$ , but above the barrier for collisions from the tip of  $^{154}\text{Sm}$ , the main contribution to the MNT processes would come from the latter, deformation aligned configuration. By carefully choosing the incident energy, one could at least investigate such a selective orientation effect on transfer processes. Decreasing the incident energy further to



the subbarrier regime for all orientations, transfer processes are dominated by quantum tunneling of nucleonic wave functions. In such a case, transfer probabilities would be more sensitive to the nature of single-particle orbitals, such as spatial distribution and angular momentum. We leave this further exploration of possible orientation effects on MNT processes in subbarrier regime as a future work.

Finally, to serve additional information on the reaction mechanism, we present a purely theoretical investigation of isotope dependence of transfer dynamics, taking the  $^{24}\text{O} + ^{154}\text{Sm}$  reaction as an example. For the  $^{16}\text{O} + ^{154}\text{Sm}$  system, neutron pickup and proton stripping are favored because of the initial  $N/Z$  asymmetry of the system. By replacing  $^{16}\text{O}$  with  $^{24}\text{O}$ , where the latter nucleus has a large  $N/Z$  ratio,  $N/Z = 2$ , we can revert the favored directions of neutron and proton transfers as compared with the  $^{16}\text{O} + ^{154}\text{Sm}$  case. This allows us to further examine effects of single-particle structures, since properties of “donor” and “acceptor” orbitals are then different. Also, it serves useful information for future experiments with neutron-rich radioactive-ion beam. For the  $^{24}\text{O} + ^{154}\text{Sm}$  system, the fusion threshold impact parameters are found to be  $b_{\text{fus}} = 5.807, 6.583, \text{ and } 5.530$  fm for  $E_{\text{c.m.}} = 77$  MeV and  $b_{\text{fus}} = 7.744, 8.961, \text{ and } 7.571$  fm for  $E_{\text{c.m.}} = 121$  MeV. These impact parameters are slightly larger than those for the  $^{16}\text{O} + ^{154}\text{Sm}$  system because of the excess neutrons in  $^{24}\text{O}$ .

In Figs. 11(b) and 11(d), we show the average numbers of transferred protons and neutrons, respectively, with respect to the projectile as a function of the impact parameter for the  $^{24}\text{O} + ^{154}\text{Sm}$  reaction at two incident energies. The incident energies were chosen to give the same center-of-mass energies as the  $^{16}\text{O} + ^{154}\text{Sm}$  reaction at  $E_{\text{lab}} = 85$  and 134 MeV. In Figs. 11(a) and 11(c), we also present the same plot for the  $^{16}\text{O} + ^{154}\text{Sm}$  system [the same data as shown in Figs. 9(c) and 9(d)] for comparison. The lower-energy case ( $E_{\text{c.m.}} = 77$  MeV) is shown by open symbols connected with dotted lines, while the higher-energy case ( $E_{\text{c.m.}} = 121$  MeV) is shown by solid symbols connected with dashed lines. Colors and symbols are the same as Fig. 9.

From the figure, one can clearly see that the directions of neutron and proton transfers are indeed reverted by replacing  $^{16}\text{O}$  with  $^{24}\text{O}$ , as expected (compare the left and right panels). From Fig. 11(b), we find that proton transfer from  $^{154}\text{Sm}$  to  $^{24}\text{O}$  is somewhat enhanced for the  $y$ -direction case (green triangles), where  $^{24}\text{O}$  collides with a point close to the tip of  $^{154}\text{Sm}$  [cf. Fig. 8(b)], which is not observed for proton transfer in the  $^{16}\text{O} + ^{154}\text{Sm}$  reaction [Fig. 11(a)]. From a careful look at neutron transfer from  $^{154}\text{Sm}$  to  $^{16}\text{O}$  shown in Fig. 11(c) a similar enhancement in the  $y$ -direction case is seen. On the other hand, from Fig. 11(d), we find that neutron transfer from  $^{24}\text{O}$  to  $^{154}\text{Sm}$  looks larger for the  $x$ - and  $z$ -direction cases, where  $^{24}\text{O}$  collides close to the equatorial side of  $^{154}\text{Sm}$  [cf. Fig. 8(a)]. A similar tendency is also observed in proton transfer from  $^{16}\text{O}$  to  $^{154}\text{Sm}$  in the  $^{16}\text{O} + ^{154}\text{Sm}$  reaction [Fig. 11(a)]. Combining these observations for the  $^{16}\text{O} + ^{154}\text{Sm}$  and  $^{24}\text{O} + ^{154}\text{Sm}$  systems, we may conclude that (i) addition of nucleons to the prolately deformed  $^{154}\text{Sm}$  may be enhanced when the projectile collides with the equatorial side of  $^{154}\text{Sm}$ , and (ii) removal of nucleons from  $^{154}\text{Sm}$  may

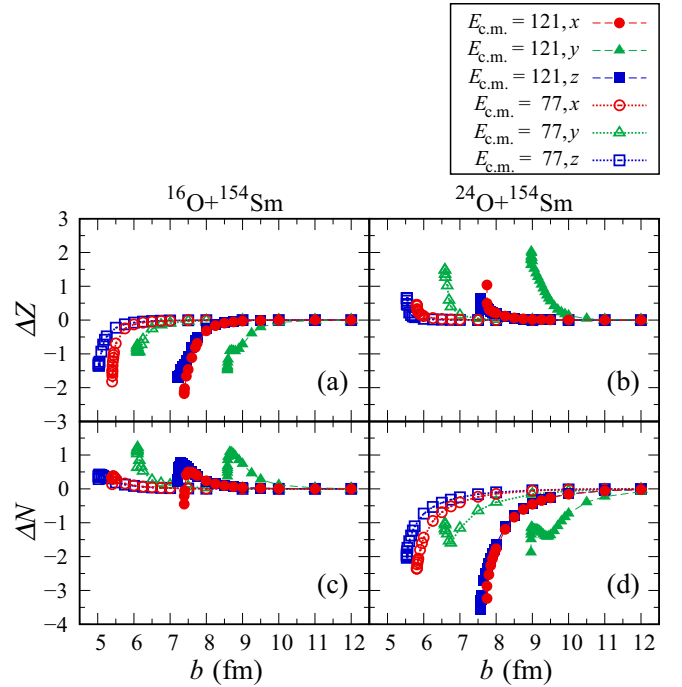


FIG. 11. Results of TDHF calculations for the  $^{16,24}\text{O} + ^{154}\text{Sm}$  reactions at  $E_{\text{c.m.}} = 77$  and 121 MeV. The average numbers of transferred protons (neutrons) are shown in upper (lower) panels as functions of the impact parameter  $b$ . Plus (minus) sign corresponds to addition to (removal from) the projectile nucleus. In the left column [panels (a) and (c)], results for the  $^{16}\text{O} + ^{154}\text{Sm}$  reaction are shown [the same data as shown in Figs. 9(c) and 9(d)], while the right column [panels (b) and (d)] shows those for the  $^{24}\text{O} + ^{154}\text{Sm}$  reaction. Results for  $E_{\text{c.m.}} = 77$  MeV are shown by open symbols connected with dotted lines, while those for  $E_{\text{c.m.}} = 121$  MeV are shown by solid symbols connected with dashed lines.

be favored when the projectile collides with the tip of  $^{154}\text{Sm}$ . Certainly, transfer dynamics reflect structural properties of donor and acceptor nuclei. By carefully choosing colliding nuclei and analyzing transfer processes, one may be able to investigate effects of single-particle orbitals as well as deformation on multinucleon transfer processes in low-energy heavy-ion reactions.

#### IV. SUMMARY

There has been a revival of interest on multinucleon transfer reactions in recent years not only as a way to investigate nucleon-nucleon correlations and single-particle properties, but also as a possible means to produce unknown neutron-rich nuclei. Since the majority of atomic nuclei manifest static deformation in their ground state, it is natural to investigate the role of mutual orientations of deformed nuclei in the multinucleon transfer mechanism.

To develop understanding of the reaction mechanism and to shed some light on the effect of nuclear orientation on multinucleon transfer processes, we have conducted experiments on the  $^{16}\text{O} + ^{154}\text{Sm}$  reaction at  $E_{\text{lab}} = 85$  MeV (near the Coulomb barrier) and 134 MeV (substantially

above the barrier), where the target nucleus  $^{154}\text{Sm}$  is a well-deformed nucleus. Angular distributions for elastic scattering and for various transfer channels as well as energy (TKEL) spectra have been measured, and  $Q$ -value- and angle-integrated isotope production cross sections have been obtained.

To understand the experimental data, the  $^{16}\text{O} + ^{154}\text{Sm}$  reaction has been analyzed based on the microscopic framework of the time-dependent Hartree-Fock (TDHF) theory. Production cross sections for various transfer channels have been obtained employing the particle-number projection method [66]. With the use of a statistical compound-nucleus deexcitation model, GEMINI++ [67–69], effects of secondary particle evaporation processes have been taken into account. From the comparison between the theoretical and the experimental results for production cross sections, we have found reasonable agreement for channels accompanying transfer of a few nucleons. For the  $E_{\text{lab}} = 85$  MeV case, however, TDHF + GEMINI underestimates production cross sections for many-nucleon transfer channels. On the other hand, we have found that cross sections for the higher-energy case ( $E_{\text{lab}} = 134$  MeV) nicely capture the trends experimentally observed for the  $E_{\text{lab}} = 85$  MeV case. The latter observation indicates possible underestimation of excitation energy of reaction products in the present TDHF + GEMINI analysis. It would be possible to improve the description by using, e.g., the stochastic mean-field (SMF) approach [57,58,73,74]. Although the present analysis certainly offers additional information on the multinucleon transfer mechanism, however, it turned out that the orientation effect is rather weak, hard to disentangle from the integrated cross sections, at least for the  $^{16}\text{O} + ^{154}\text{Sm}$  reaction at the two incident energies examined.

Although we could not see clear orientation effects in the integrated cross sections, some symptom of orientation dependence of transfer dynamics has been observed in TDHF calculations for the  $^{16,24}\text{O} + ^{154}\text{Sm}$  reactions, where the  $^{24}\text{O} + ^{154}\text{Sm}$  system was additionally analyzed to explore isotope as well as orientation dependence of transfer mechanism within the TDHF approach. As is naively expected,

there is a simple geometric effect on reaction dynamics, which makes reactions take place at larger impact parameters when the deformation axis of  $^{154}\text{Sm}$  is set aligned to the impact-parameter vector. Apart from the geometric effect, we have found that (i) addition of nucleons to the prolately deformed  $^{154}\text{Sm}$  (or tendency towards fusion) may be enhanced when the projectile collides with the equatorial side of  $^{154}\text{Sm}$ , and (ii) removal of nucleons from  $^{154}\text{Sm}$  may be favored when the projectile collides with the tip of  $^{154}\text{Sm}$ . Although we could not disentangle such orientation effects from the present experimental data, as a future work one may explore the subbarrier energy regime where data would be sensitive to single-particle properties.

## ACKNOWLEDGMENTS

The staff of BARC-TIFR Pelletron-Linac facility, Mumbai, is highly appreciated for their excellent support during the beam time. We are thankful to Dr. Rahul Tripathy and Dr. T.N. Nag, Radio Chemistry Division, BARC, Mumbai, for providing aluminium target and preparing the samarium target for us. We thank Dr. A.K. Mohanty, Dr. P.P. Singh, Dr. T. Sinha, Dr. V. Jha, Dr. A. Kundu, Dr. D. Chattopadhyay, Dr. Sonika, and Dr. A. Parmar for their help during the beam time and interest during the initial stages of this work. One of the authors (B.J.R.) is thankful to a project trainee Nitika for her involvement in some parts of the data analysis as a part of her internship work. We also thank Harun Al Rashid for his interest and contribution to this work. Theoretical calculations were performed using computational resources of the HPCI system (Oakforest-PACS) provided by Joint Center for Advanced High Performance Computing (JCAHPC) through the HPCI System Project (Project ID: hp210023). This work also used (in part) computational resources of the Yukawa-21 System at Yukawa Institute for Theoretical Physics (YITP), Kyoto University. One of the authors (K.S.) was supported by the Japan Society for the Promotion of Science (JSPS) KAKENHI, Grant-in-Aid for Early-Career Scientists, Grant No. 19K14704.

- 
- [1] K. Hagino and N. Takigawa, Subbarrier fusion reactions and many-particle quantum tunneling, *Prog. Theor. Phys.* **128**, 1061 (2012).
- [2] A. Wakhle, C. Simenel, D. J. Hinde, M. Dasgupta, M. Evers, D. H. Luong, R. du Rietz, and E. Williams, Interplay between Quantum Shells and Orientation in Quasifission, *Phys. Rev. Lett.* **113**, 182502 (2014).
- [3] V. E. Oberacker, A. S. Umar, and C. Simenel, Dissipative dynamics in quasifission, *Phys. Rev. C* **90**, 054605 (2014).
- [4] A. S. Umar, V. E. Oberacker, and C. Simenel, Shape evolution and collective dynamics of quasifission in the time-dependent Hartree-Fock approach, *Phys. Rev. C* **92**, 024621 (2015).
- [5] K. Sekizawa and K. Yabana, Time-dependent Hartree-Fock calculations for multinucleon transfer and quasifission processes in the  $^{64}\text{Ni} + ^{238}\text{U}$  reaction, *Phys. Rev. C* **93**, 054616 (2016).
- [6] A. S. Umar, V. E. Oberacker, and C. Simenel, Fusion and quasifission dynamics in the reactions  $^{48}\text{Ca} + ^{249}\text{Bk}$  and  $^{50}\text{Ti} + ^{249}\text{Bk}$  using a time-dependent Hartree-Fock approach, *Phys. Rev. C* **94**, 024605 (2016).
- [7] H. Zheng, S. Burrello, M. Colonna, D. Lacroix, and G. Scamps, Connecting the nuclear equation of state to the interplay between fusion and quasifission processes in low-energy nuclear reactions, *Phys. Rev. C* **98**, 024622 (2018).
- [8] L. Guo, C. Shen, C. Yu, and Z. Wu, Isotopic trends of quasifission and fusion-fission in the reactions  $^{48}\text{Ca} + ^{239,244}\text{Pu}$ , *Phys. Rev. C* **98**, 064609 (2018).
- [9] K. Godbey, A. S. Umar, and C. Simenel, Deformed shell effects in  $^{48}\text{Ca} + ^{249}\text{Bk}$  quasifission fragments, *Phys. Rev. C* **100**, 024610 (2019).
- [10] D. J. Kedziora and C. Simenel, New inverse quasifission mechanism to produce neutron-rich transfermium nuclei, *Phys. Rev. C* **81**, 044613 (2010).
- [11] K. Sekizawa, Enhanced nucleon transfer in tip collisions of  $^{238}\text{U} + ^{124}\text{Sn}$ , *Phys. Rev. C* **96**, 041601(R) (2017).

- [12] L. Corradi, G. Pollarolo, and S. Szilner, Multinucleon transfer processes in heavy-ion reactions, *J. Phys. G* **36**, 113101 (2009).
- [13] F.-S. Zhang, C. Li, L. Zhu, and P. Wen, Production cross sections for exotic nuclei with multinucleon transfer reactions, *Front. Phys.* **13**, 132113 (2018).
- [14] K. Sekizawa, Time-dependent Hartree-Fock theory and its extensions for the multinucleon transfer reactions: A mini review, *Front. Phys.* **7**, 20 (2019).
- [15] G. G. Adamian, N. V. Antonenko, A. Diaz-Torres, and S. Heinz, How to extend the chart of nuclides?, *Eur. Phys. J. A* **56**, 47 (2020).
- [16] V. Zagrebaev and W. Greiner, Production of New Heavy Isotopes in Low-Energy Multinucleon Transfer Reactions, *Phys. Rev. Lett.* **101**, 122701 (2008).
- [17] V. I. Zagrebaev and W. Greiner, Production of heavy and super-heavy neutron-rich nuclei in transfer reactions, *Phys. Rev. C* **83**, 044618 (2011).
- [18] V. I. Zagrebaev and W. Greiner, Production of heavy trans-target nuclei in multinucleon transfer reactions, *Phys. Rev. C* **87**, 034608 (2013).
- [19] A. V. Karpov and V. V. Saiko, Modeling near-barrier collisions of heavy ions based on a Langevin-type approach, *Phys. Rev. C* **96**, 024618 (2017).
- [20] V. V. Saiko and A. V. Karpov, Analysis of multinucleon transfer reactions with spherical and statically deformed nuclei using a Langevin-type approach, *Phys. Rev. C* **99**, 014613 (2019).
- [21] L. Zhu, Z.-Q. Feng, and F.-S. Zhang, Production of heavy neutron-rich nuclei in transfer reactions within the dinuclear system model, *J. Phys. G* **42**, 085102 (2015).
- [22] L. Zhu, J. Su, W.-J. Xie, and F.-S. Zhang, Production of neutron-rich transcalifornium nuclei in  $^{238}\text{U}$ -induced transfer reactions, *Phys. Rev. C* **94**, 054606 (2016).
- [23] L. Zhu, J. Su, W.-J. Xie, and F.-S. Zhang, Theoretical study on production of heavy neutron-rich isotopes around the  $N = 126$  shell closure in radioactive beam induced transfer reactions, *Phys. Lett. B* **767**, 437 (2017).
- [24] L. Zhu, F.-S. Zhang, P.-W. Wen, J. Su, and W.-J. Xie, Production of neutron-rich nuclei with  $Z = 60\text{--}73$  in reactions induced by Xe isotopes, *Phys. Rev. C* **96**, 024606 (2017).
- [25] Z.-Q. Feng, Production of neutron-rich isotopes around  $N = 126$  in multinucleon transfer reactions, *Phys. Rev. C* **95**, 024615 (2017).
- [26] G. Zhang, C. Li, P.-W. Wen, J.-J. Li, X.-X. Xu, B. Li, Z. Liu, and F.-S. Zhang, Production of neutron-rich  $^{209\text{--}212}\text{Pt}$  isotopes based on a dinuclear system model, *Phys. Rev. C* **98**, 014613 (2018).
- [27] P.-H. Chen, F. Niu, W. Zuo, and Z.-Q. Feng, Approaching the neutron-rich heavy and superheavy nuclei by multinucleon transfer reactions with radioactive isotopes, *Phys. Rev. C* **101**, 024610 (2020).
- [28] K. Zhao, Z. Li, N. Wang, Y. Zhang, Q. Li, Y. Wang, and X. Wu, Production mechanism of neutron-rich transuranium nuclei in  $^{238}\text{U} + ^{238}\text{U}$  collisions at near-barrier energies, *Phys. Rev. C* **92**, 024613 (2015).
- [29] N. Wang and L. Guo, New neutron-rich isotope production in  $^{154}\text{Sm} + ^{160}\text{Gd}$ , *Phys. Lett. B* **760**, 236 (2016).
- [30] K. Zhao, Z. Li, Y. Zhang, N. Wang, Q. Li, C. Shen, Y. Wang, and X. Wu, Production of unknown neutron-rich isotopes in  $^{238}\text{U} + ^{238}\text{U}$  collisions at near-barrier energy, *Phys. Rev. C* **94**, 024601 (2016).
- [31] C. Li, X. Xu, J. Li, G. Zhang, B. Li, C. A. T. Sokhna, Z. Ge, F. Zhang, P. Wen, and F.-S. Zhang, Production of new neutron-rich heavy nuclei with  $Z = 56\text{--}80$  in the multinucleon transfer reactions of  $^{136}\text{Xe} + ^{198}\text{Pt}$ , *Phys. Rev. C* **99**, 024602 (2019).
- [32] K. Zhao, Z. Liu, F. S. Zhang, and N. Wang, Production of neutron-rich  $N = 126$  nuclei in multinucleon transfer reactions: Comparison between  $^{136}\text{Xe} + ^{198}\text{Pt}$  and  $^{238}\text{U} + ^{198}\text{Pt}$  reactions, *Phys. Lett. B* **815**, 136101 (2021).
- [33] Y. X. Watanabe, Y. H. Kim, S. C. Jeong, Y. Hirayama, N. Imai, H. Ishiyama, H. S. Jung, H. Miyatake, S. Choi, J. S. Song, E. Clement, G. de France, A. Navin, M. Rejmund, C. Schmitt, G. Pollarolo, L. Corradi, E. Fioretto, D. Montanari, M. Niikura *et al.*, Pathway for the Production of Neutron-Rich Isotopes around the  $N = 126$  Shell Closure, *Phys. Rev. Lett.* **115**, 172503 (2015).
- [34] S. Hofmann and G. Münzenberg, The discovery of the heaviest elements, *Rev. Mod. Phys.* **72**, 733 (2000).
- [35] Y. T. Oganessian, A. Sobiczewski, and G. M. Ter-Akopian, Superheavy nuclei: From predictions to discovery, *Phys. Scr.* **92**, 023003 (2017).
- [36] T. Otsuka, A. Gade, O. Sorlin, T. Suzuki, and Y. Utsuno, Evolution of nuclear structure in exotic nuclei and nuclear forces, *Rev. Mod. Phys.* **92**, 015002 (2020).
- [37] P. Cejnar, J. Jolie, and R. F. Casten, Quantum phase transitions in the shapes of atomic nuclei, *Rev. Mod. Phys.* **82**, 2155 (2010).
- [38] K. Heyde and J. L. Wood, Shape coexistence in atomic nuclei, *Rev. Mod. Phys.* **83**, 1467 (2011) [**83**, 1655(E) (2011)].
- [39] H. Sakurai, Nuclear physics with RI beam factory, *Front. Phys.* **13**, 132111 (2018); see also <http://www.nishina.riken.jp/RIBF/>.
- [40] <http://english.imp.cas.cn/Home2017/>.
- [41] T. Shin, B. H. Kang, G. D. Kim, Y. J. Kim, Y. K. Kwon, Y. H. Park, K. Tshoo, and C. C. Yun, Rare isotope production and experimental systems of RAON, *Sae Mulli* **66**, 1500 (2016).
- [42] S. Gales, SPIRAL2 at GANIL A world leading ISOL facility at the dawn of the next decade, *Prog. Part. Nucl. Phys.* **59**, 22 (2007); see also <https://www.ganil-spiral2.eu/> for information about SPIRAL2 at GANIL.
- [43] For information about FAIR (Facility for Antiproton and Ion Research in Europe) at GSI, see <https://fair-center.eu/>.
- [44] For information about SPES (Selective Production of Exotic Species) at INFN-LNL, see <https://web.infn.it/spes/>.
- [45] E. P. Abel *et al.*, Isotope Harvesting at FRIB: Additional opportunities for scientific discovery, *J. Phys. G Nucl. Part. Phys.* **46**, 100501 (2019); see also: <https://frib.msu.edu/>.
- [46] Sonika, B. J. Roy, A. Parmar, U. K. Pal, H. Kumawat, V. Jha, S. K. Pandit, V. V. Parkar, K. Ramachandran, K. Mahata, A. Pal, S. Santra, A. K. Mohanty, and K. Sekizawa, Multinucleon transfer study in  $^{206}\text{Pb}(^{18}\text{O}, x)$  at energies above the Coulomb barrier, *Phys. Rev. C* **92**, 064902 (2015).
- [47] B. J. Roy, Y. Sawant, P. Patwari, S. Santra, A. Pal, A. Kundu, D. Chattopadhyay, V. Jha, S. K. Pandit, V. V. Parkar, K. Ramachandran, K. Mahata, B. K. Nayak, A. Saxena, S. Kailas, T. N. Nag, R. N. Sahoo, P. P. Singh, and K. Sekizawa, Deep-inelastic multinucleon transfer processes in the  $^{16}\text{O} + ^{27}\text{Al}$  reaction, *Phys. Rev. C* **97**, 034603 (2018).
- [48] Database NuDat3.0 provided by National Nuclear Data Center, Brookhaven National Laboratory, <https://www.nndc.bnl.gov/nudat3/>.
- [49] I. J. Thompson, Coupled reaction channels calculations in nuclear physics, *Comput. Phys. Rep.* **7**, 167 (1988); see also

- <http://www.fresco.org.uk> for details of the computer program, SFRESCO.
- [50] K. Sekizawa and K. Yabana, Time-dependent Hartree-Fock calculations for multinucleon transfer processes in  $^{40,48}\text{Ca} + ^{124}\text{Sn}$ ,  $^{40}\text{Ca} + ^{208}\text{Pb}$ , and  $^{58}\text{Ni} + ^{208}\text{Pb}$  reactions, *Phys. Rev. C* **88**, 014614 (2013) [**93**, 029902(E) (2016)].
- [51] K. Sekizawa and K. Yabana, Particle-number projection method in time-dependent Hartree-Fock theory, *Phys. Rev. C* **90**, 064614 (2014).
- [52] K. Sekizawa and S. Heinz, Quasifission dynamics and stability of superheavy systems, *Acta Phys. Pol. B* **10**, 225 (2017).
- [53] K. Sekizawa, Microscopic description of production cross sections including deexcitation effects, *Phys. Rev. C* **96**, 014615 (2017).
- [54] K. Washiyama and K. Sekizawa, TDHF and a macroscopic aspect of low-energy nuclear reactions, *Front. Phys.* **8**, 93 (2020).
- [55] E. Williams, K. Sekizawa, D. J. Hinde, C. Simenel, M. Dasgupta, I. P. Carter, K. J. Cook, D. Y. Jeung, S. D. McNeil, C. S. Palshetkar, D. C. Rafferty, K. Ramachandran, and A. Wakhle, Exploring Zeptosecond Quantum Equilibration Dynamics: From Deep-Inelastic to Fusion-Fission Outcomes in  $^{58}\text{Ni} + ^{60}\text{Ni}$  Reactions, *Phys. Rev. Lett.* **120**, 022501 (2018).
- [56] K. Sekizawa and K. Hagino, Time-dependent Hartree-Fock plus Langevin approach for hot fusion reactions to synthesize the  $Z = 120$  superheavy element, *Phys. Rev. C* **99**, 051602(R) (2019).
- [57] K. Sekizawa and S. Ayik, Quantal diffusion approach for multinucleon transfer processes in the  $^{58,64}\text{Ni} + ^{208}\text{Pb}$  reactions: Toward the production of unknown neutron-rich nuclei, *Phys. Rev. C* **102**, 014620 (2020).
- [58] S. Ayik and K. Sekizawa, Kinetic energy dissipation and fluctuations in strongly-damped heavy-ion collisions within the stochastic mean-field approach, *Phys. Rev. C* **102**, 064619 (2020).
- [59] J. W. Negele, The mean-field theory of nuclear structure and dynamics, *Rev. Mod. Phys.* **54**, 913 (1982).
- [60] C. Simenel, Nuclear quantum many-body dynamics, *Eur. Phys. J. A* **48**, 152 (2012).
- [61] T. Nakatsukasa, Density functional approaches to collective phenomena in nuclei: Time-dependent density functional theory for perturbative and nonperturbative nuclear dynamics, *Prog. Theor. Exp. Phys.* **2012**, 01A207 (2012).
- [62] T. Nakatsukasa, K. Matsuyanagi, M. Matsuo, and K. Yabana, Time-dependent density-functional description of nuclear dynamics, *Rev. Mod. Phys.* **88**, 045004 (2016).
- [63] C. Simenel and A. S. Umar, Heavy-ion collisions and fission dynamics with the time-dependent Hartree-Fock theory and its extensions, *Prog. Part. Nucl. Phys.* **103**, 19 (2018).
- [64] P. D. Stevenson and M. C. Barton, Low-energy heavy-ion reactions and the Skyrme effective interaction, *Prog. Part. Nucl. Phys.* **104**, 142 (2019).
- [65] E. Chabanat, P. Bonche, P. Haensel, J. Meyer, and R. Schaeffer, A Skyrme parametrization from subnuclear to neutron star densities Part II. Nuclei far from stabilities, *Nucl. Phys. A* **635**, 231 (1998); **643**, 441 (1998).
- [66] C. Simenel, Particle Transfer Reactions with the Time-Dependent Hartree-Fock Theory Using a Particle Number Projection Technique, *Phys. Rev. Lett.* **105**, 192701 (2010).
- [67] R. J. Charity, GEMINI: A Code to Simulate the Decay of a Compound Nucleus by a Series of Binary Decays, in *Joint ICTP-AIEA Advanced Workshop on Model Codes for Spallation Reactions*, Report INDC(NDC)-0530 (IAEA, Vienna, 2008), p. 139.
- [68] R. J. Charity, Systematic description of evaporation spectra for light and heavy compound nuclei, *Phys. Rev. C* **82**, 014610 (2010).
- [69] D. Mancusi, R. J. Charity, and J. Cugnon, Unified description of fission in fusion and spallation reactions, *Phys. Rev. C* **82**, 044610 (2010).
- [70] W. J. Huang, M. Wang, F. G. Kondev, G. Audi, and S. Naimi, The AME 2020 atomic mass evaluation (I). Evaluation of input data, and adjustment procedures, *Chin. Phys. C* **45**, 030002 (2021).
- [71] M. Wang, W. J. Huang, F. G. Kondev, G. Audi, and S. Naimi, The AME 2020 atomic mass evaluation (II). Tables, graphs and references, *Chin. Phys. C* **45**, 030003 (2021).
- [72] R. Balian and M. Vénéroni, Time-Dependent Variational Principle for Predicting the Expectation Value of an Observable, *Phys. Rev. Lett.* **47**, 1353 (1981) [**47**, 1765(E) (1981)].
- [73] S. Ayik, A stochastic mean-field approach for nuclear dynamics, *Phys. Lett. B* **658**, 174 (2008).
- [74] D. Lacroix and S. Ayik, Stochastic quantum dynamics beyond mean field, *Eur. Phys. J. A* **50**, 95 (2014).